**V.M. Gun'ko [1], B. Charmas [2], J. Skubiszewska–Zięba [2]**

# NANOSTRUCTURED COMPOSITES WITH PRECIPITATED SILICA – Ni CRYSTALLITES COATED BY CHAR WITH CARBONIZED STARCH

*[1] Chuiko Institute of Surface Chemistry of National Academy of Sciences of Ukraine*
*17 General Naumov Str., Kyiv, 03164, Ukraine, E-mail: vlad_gunko@ukr.net*
*[2] Faculty of Chemistry, Maria Curie–Skłodowska University*
*3 Maria Curie–Skłodowska Sq., Lublin, 20–031, Poland*

*Hybrid carbons/metals/metal (metalloid) oxides composites could be effective adsorbents for low– and high– molecular weight compounds, polar and nonpolar, gaseous and liquid. The presence of metal nanocrystallites and carbon nanostructures could provide catalytic properties in redox reactions. For more effective use of hybrid composites, their morphological, structural, textural, and adsorption characteristics should be appropriate for target applications and, therefore, well controlled. Therefore, the aim of this study was to synthesize carbon/metal/silica nanostructured composites with varied content of metal (Ni) to control the mentioned characteristics. Precipitated silica Sipernat 50 was selected as a substrate. Potato starch was used as a carbon precursor. Nickel nitrate (Ni(NO$_3$)$_2$·6H$_2$O) of varied amounts was used as a precursor of Ni nanoparticles reduced upon the starch carbonization. After the starch carbonization and Ni reduction, a set of C/Ni/silica samples was studied using atomic force microscopy, X–ray diffraction, X–ray fluorescence spectroscopy, nitrogen and p-nitrophenol adsorption, thermogravimetry, and Raman spectroscopy. The presence of nickel phase results in the formation of smaller but denser packed char nanoparticles. Estimation of possible contribution of pores accessible for nitrogen molecules in silica globules and outer surface of carbon/Ni particles suggests that the carbon phase is porous that provides a significant part of the specific surface area of the composites. Amorphous silica and char phases are characterized by the presence of certain nuclei of radius (R) < 1 nm and 2 nm < R < 10 nm estimated from the XRD patterns using full peak profile analysis with a self–consistent regularization procedure. Ni crystallites are of several sizes, since particle size distributions include two–three peaks in the range of 3–13 nm in radius. The Raman spectra show that the main changes with increasing Ni content are characteristic to sp$^3$ carbon structures (D line) in contrast to the sp$^2$ structures (G line). The pore size distributions (both differential and incremental) demonstrate complex changes in a broad size range due to increasing Ni content in composites. As a whole, changes in the Ni content in nanostructured C/Ni/silica composites allow one to control the morphological, structural, and textural characteristics of the whole materials.*

*Keywords: precipitated silica, starch, nickel nitrate, Ni nanocrystallites, char–covered Ni nanoparticles, structural characteristics*

## INTRODUCTION

Hybrid adsorbents composed of inorganics/organics, metal oxides/carbons, metal/metal oxides/carbons and other various components are of interest due to widening of the characteristics and properties of composites and certain synergetic effects in comparison to individual materials that are important for practical applications [1–14]. For example, carbon–mineral composites can be more effective as adsorbents, catalysts, fillers, *etc.* than the corresponding individual carbons and mineral materials. However, transformation of organics into carbonaceous deposits (coke, char, pyrocarbon) at a surface of catalysts can be a negative factor because the deposits inhibit

catalytic reactions on active surface sites due to their blocking. On the other hand, carbon structures (nanoparticles, clusters, thin films) immobilized at a surface of solid supports can be interesting as catalysts and adsorbents per se or as important components of hybrid adsorbents, fillers, and catalysts [1–7], which can be applied in chromatography [14], trace analysis or as catalyst supports, *etc.* [1, 15–30]. There are various carbons used as components of hybrid composites, *e.g.*, carbon nanotubes – silicas [1, 15–17], graphite or graphite oxide – silica, activated carbon – silica, hybrid aerogels, ordered mesoporous silicas – carbons including replicas, graphene or graphene oxide – metal (metalloid) oxides, carbon – silica membranes, composites with carbon nanofibers, or more complex

V.M. Gun'ko, B. Charmas, J. Skubiszewska–Zięba

composites [1–14, 18–44]. Some of carbon – silica materials were prepared by polymerization of components or precursors (such as polymers) simultaneously and then by carbonization of organics. Carbon – silica materials can be used not only in industrial, lab, and scientific applications but also in biomedical applications [1]. Thus, carbon – mineral adsorbents are widely known materials due to their potential applicability to laboratory and industrial purposes, trace analysis, catalysis, environmental protection, sewage purification, *etc.* Their structural characteristics and chemical properties can be easily changed due to a variety of carbon and mineral precursors used for their preparation. Moreover, to differentiate their surface structures, there exist many methods of modifications such as hydrothermal treatment, grafting of different polymers or functionalities, introduction of heteroatoms, such as N, S, or P, *etc.* For catalytic applications of carbon–mineral composites, there is an important factor such as the presence of metal species of appropriate crystallinity and dispersion. Note that previously, some carbon–mineral adsorbents were studied in detail [45–59]. On the basis of these studies, one could assume that the presence of metals and metal oxides in the

carbonization products, *e.g.*, core–shell particles, could lead to significant changes in the composite structures, characteristics, and properties. To elucidate morphological, structural, and textural features of the complex systems, a set of experimental methods should be used and the experimental data should be treated using appropriately developed software. Therefore, the aim of this work was to prepare silica – Ni/carbon composites with developed porous structure at different amounts of Ni and appropriately studied and analyzed.

MATERIALS

Precipitated silica Sipernat 50 (Si–50, $S_{BET} = 503$ m$^2$/g, average particle size $d \approx 50$ μm, tamped density 175 g/dm$^3$, Evonik, Germany), commercial potato starch (Polish) as a carbon precursor, and Ni(NO$_3$)$_2 \cdot 6H_2O$ (Merck) as a precursor of Ni particles were used to prepare a set of composite samples. A series of carbon–silica samples with different content of nickel was prepared using various quantities (from 0 to 2.5 mmol of the salt giving labels of samples from CS–Ni–0 to CS–Ni–2.5, Table 1).

**Table 1.** Characteristics of composites with different content of nickel

| Sample | $C_C$ (wt. %) | $C_{Ni}$ (wt. %) | $C_{SiO2}$ (wt. %) | Average size of Ni crystallites (nm) |
|---|---|---|---|---|
| CS–Ni–0 | 18.0 | – | 82.0 | – |
| CS–Ni–0.5 | 19.0 | 2.86 | 78.14 | 6.80 |
| CS–Ni–1 | 15.3 | 5.43 | 79.27 | 8.28 |
| CS–Ni–1.5 | 14.6 | 7.91 | 77.49 | 7.20 |
| CS–Ni–2 | 11.8 | 10.34 | 77.86 | 6.75 |
| CS–Ni–2.5 | 11.5 | 12.66 | 75.84 | 7.06 |

*Note.* $C_C$ was determined using TG data; $C_{Ni}$ was estimated from XRF data; Ni crystallite sizes were computed from the XRD data using the Scherrer equation

Appropriate weights of nickel nitrate were poured into a beaker with a capacity of 250 cm$^3$, followed by 95 cm$^3$ of distilled water. After dissolving the nickel salt in water, starch (2.7 grams) and silica (3 grams) were poured into the solution. It was sonicated and heated for starch gelatinization at 69 °C (with continuous stirring) and maintained at this temperature for 1 h. Then it was poured onto aluminium foil with a large surface allowed to dry the mixture at room temperature for 24 h. The dried samples were ground in a mortar and then sieved through

sieves with a mesh size of 0.2 mm and 0.16 mm. Then it was subjected to pyrolysis at 500 °C in the nitrogen atmosphere in a quartz rotary reactor for 3 h. The composite samples (Table 1) were studied using nitrogen adsorption, X–ray diffraction (XRD), spectral (Raman, XRF), thermal (TG, DTA), and microscopy (AFM) methods. Note that there is a tendency of decreasing char content and increasing Ni content with increasing amounts of nickel nitrate in the reaction blends (Table 1).

## CHARACTERIZATION METHODS

The nitrogen adsorption/desorption isotherms were recorded at 77.4 K using a Micromeritics ASAP 2405N adsorption analyzer. The specific surface area, $S_{BET}$ was calculated using the standard BET equation [60] at $p/p_0$ between 0.06 and 0.2 (where $p$ and $p_0$ denote the equilibrium and saturation pressures of nitrogen, respectively). The pore volume ($V_p$) was estimated under the relative pressure $p/p_0 \approx 0.98$ [61]. The nitrogen desorption data were used to compute the pore size distributions (PSD, differential $f_V(R) \sim dV_p/dR$ and $f_S(R) \sim dS/dR$) using a self–consistent regularization (SCR) procedure under non–negativity condition ($f_V(R) \geq 0$ at any pore radius $R$) at a fixed regularization parameter $\alpha = 0.01$. A complex pore model was applied with slit–shaped (S) pores in carbon and cylindrical (C) pores in silica and voids (V) between spherical carbon nanoparticles packed in random aggregates (SCV/SCR method) [62–64]. The differential PSD with respect to the pore volume $f_V(R) \sim dV/dR$, $\int f_V(R)dR \sim V_p$ were re–calculated to incremental PSD (IPSD) at $\Phi_V(R_i) = (f_V(R_{i+1}) + f_V(R_i))(R_{i+1} - R_i)/2$ at $\sum \Phi_V(R_i) = V_p$. The $f_V(R)$ and $f_S(R)$ functions were also used to calculate contributions of nanopores ($V_{nano}$ and $S_{nano}$ at radius in the range of 0.35 nm $< R <$ 1 nm), mesopores ($V_{meso}$ and $S_{meso}$ at 1 nm $< R <$ 25 nm), and macropores ($V_{macro}$ and $S_{macro}$ at 25 nm $< R <$ 100 nm) [62]. Additionally, non–local density functional theory (NLDFT, Quantachrome software, with a model of cylindrical pores in silica or slit/cylindrical pores in carbon) method [65] was used to calculate the differential PSD and converted to the IPSD. The average values of the pore radii $<R_X>$ could be determined with respect to the pore volume (X = V) and specific surface area (X = S), respectively, as the ratio of the first and zero moments of the distribution functions

$$< R_X > = \int_{R_{min}}^{R_{max}} R f_X(R)dR / \int_{R_{min}}^{R_{max}} f_X(R)dR. \quad (1)$$

Additionally, $f_S(R)$ could be used to estimate the deviation ($\Delta w$) of the pore shape from the model using [62, 66, 67]

$$\Delta w = S_{BET} / \int_{R_{min}}^{R_{max}} f_S(R)dR - 1, \quad (2)$$

where $R_{max}$ and $R_{min}$ are the maximal and minimal pore radii respectively. The $S^*_{nano}$, $S^*_{meso}$ and $S^*_{macro}$ values could be corrected by multiplication by ($\Delta w$+1) that gives $S^*(\Delta w+ 1) = S_{sum} = S_{nano} + S_{meso} + S_{macro} = S_{BET}$. The effective $w$ value ($w_{ef}$) can be estimated with equation

$$w_{ef} = (S_{BET} / V_p) \int_{R_{min}}^{R_{max}} R f_V(R)dR / \int_{R_{min}}^{R_{max}} f_V(R)dR. \quad (3)$$

However, the reliability of the $\Delta w$ value depends on the reliability of both $S_{BET}$ and PSD.

Thermogravimetry (TG) with differential thermal analysis (DTA) was carried out in air at 20–1000 ºC using a Q apparatus (Derivatograph–C, Paulik, Paulik & Erdey, MOM, Budapest) at a heating rate of 10 K/min.

Atomic Force Microscopic (AFM) images were obtained by means of a NanoScope III (Digital Instruments, USA) apparatus using a tapping mode AFM measurement technique. The particle size distribution (PaSD) functions using AFM images were computed using ImageJ software with a granulometry plugin [68].

X–ray diffraction (XRD) measurements were performed using a Siemens D 5000 powder diffractometer with Cu$K_a$ radiation in step scan mode (2θ step size 0.04°, counting time 2 s per step, 2θ range of 2–80° but shown in the range of 10–70°). To identify the structure of synthesized deposits, obtained patterns were compared to those of known compounds from the JPCDS–ISDD files. A method used for calculations of the size distribution functions of nanoparticles on the basis of selected XRD peaks using the SCR procedure with a complex model of particle shapes (lamellar, cylindrical, and spherical ones) was described in detail elsewhere [69].

Ni concentration was determined using a X–ray fluorescence (XRF, Canberra, Bergenfield, USA) spectrometer with the radioactive sources of $^{55}$Fe and $^{109}$Cd (Table 1).

Raman spectra were recorded using a Raman microscopy (inVia Reflex Renishaw, UK).

## RESULTS AND DISCUSSION

Water desorption from the composites gives the first weight loss around 100 °C (Fig. 1). An increase in sample weight around 300 °C is due to oxidation reactions of the composites (carbons) with oxygen/water from the air atmosphere. This effect is maximal at the absence of nickel, and it

*V.M. Gun'ko, B. Charmas, J. Skubiszewska–Zięba*

is practically absent at the maximal Ni amount (Fig. 1 *a*, *b*). These results could be explained by different structures of carbon nanoparticles affected by Ni. For example, carbon structures become more densely packed in smaller particles with increasing Ni content (Figs. 2 and 3) that are strongly bound to nickel nanoparticles. This results in decreasing their reactivity in oxidation at temperatures around 300 °C but increasing reactivity around 400 °C (Fig. 1). At higher temperatures, there are two stages (around 400 and 500 °C) with decreasing sample mass and burning char phase (Fig. 1).
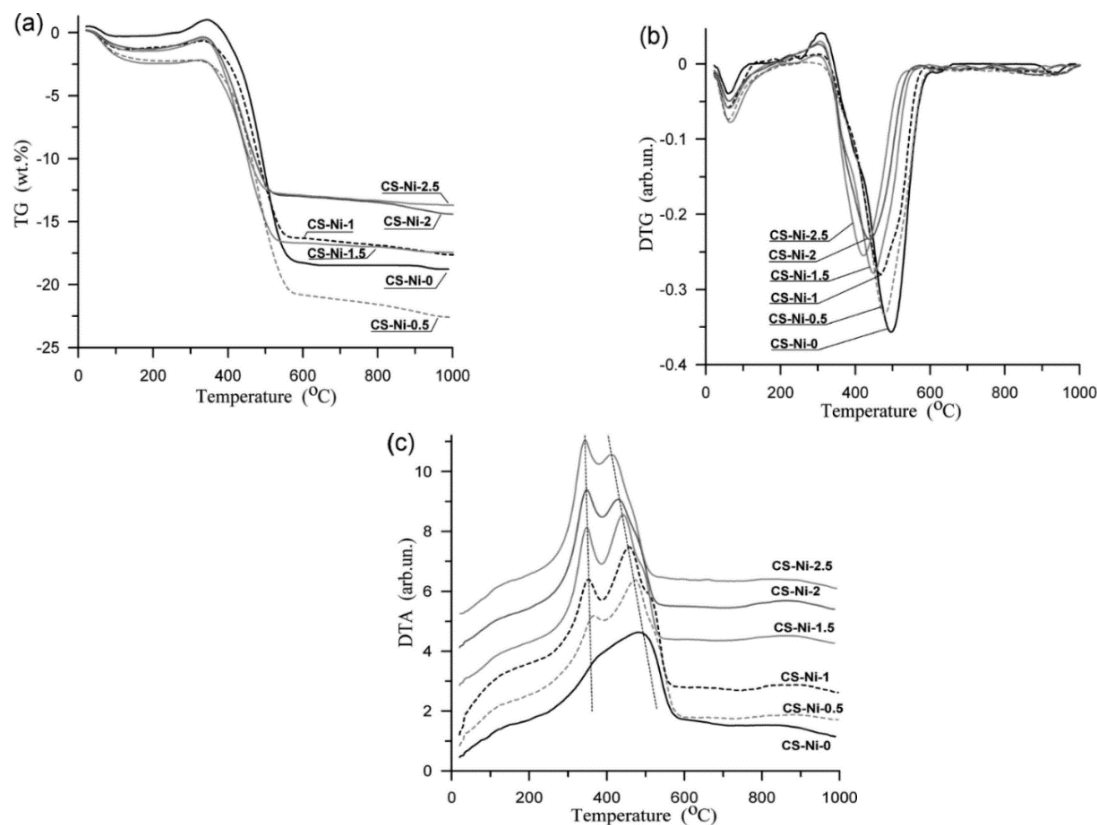


**Fig. 1.** *a* – Thermogravimetric (TG) curves, *b* – differential TG (DTG), and *c* – differential thermal analysis (DTA) curves for silica – Ni/carbon composites

The first burning stage around 400 °C is rather linked to oxidation of carbon structures of smaller sizes and bound to Ni particles (since Ni can catalyze the redox reactions) because the DTA peak is practically absent at 400 °C for CS–Ni–0 and it is maximal for CS–Ni–2.5 (Fig. 1 *c*). Additionally, the second DTA peak around 500 °C shifts toward lower temperatures with increasing Ni content.

The Ni particles include crystallites (Fig. 4) of sizes non–monotonically changing with $C_{Ni}$ (Table 1, Fig. 5 *b*). These changes could be explained by several factors: (i) changes in a ratio of starch/Ni nitrate; (ii) changes in a ratio of Si–50/Ni nitrate affecting (iii) reduction of Ni salt to metal, (iv) carbonization of starch, and (v) formation of Ni and carbon structures (Figs. 1–12,

Tables 1–4). Computation of the PaSD of nuclei in amorphous structures (including carbon and silica) using broad XRD halo line at $2\theta = 10–30°$ (Fig. 4) gives two peaks (Fig. 5 *a*).

One could assume that initial silica contribution does not practically change (during carbonization, since $C_{SiO2}$ is in a narrow range from 76 to 82 wt. %) upon changes in the Ni content, and all changes (Fig. 5 *a*) are due to changes in amorphous carbon structures, since Ni is crystalline. A maximal contribution of small nuclei at $R < 1$ nm (Fig. 5 *a*) and minimal one for larger nuclei (graphene clusters) at 2 nm $< R <$ 10 nm is for CS–Ni–0.5, and this sample is characterized by maximal sizes of Ni crystallites (Fig. 5 *b*). Note that similar nuclei and graphene

clusters are observed in high–resolution TEM images of various carbons [64, 70, 71].

The opposite results compared to those for CS–Ni–0 and CS–Ni–0.5 are observed for CS–Ni–2.5 (Fig. 5 *a*) characterized by minimal sizes of Ni crystallites (Fig. 5 *b*). Therefore, one could assume that carbon structures free of Ni form with the clusters at $R < 1$ nm, but larger carbon structures at $2$ nm $< R < 10$ nm form around Ni crystallites. Note that Ni crystallites are of several sizes, since the PaSD include two–three peaks (Fig. 5 *b*). Additionally, some Ni particles could include several small crystallites, as well as carbon shell around Ni nanoparticle could be composed with several graphene clusters. Therefore, the Scherrer equation gives results for Ni crystallite sizes (Table 1) different from those obtained using the full profile analysis of the main XRD peaks with the SCR procedure. Additionally, the shapes of nanoparticles change with increasing Ni content (Table 2). For example, contribution of spherical char particles (as in carbon black) decreases and contribution of lamellar structures is maximal at maximal $C_{Ni}$ value, but for Ni particles, contribution of spherical particles (as an appropriate model of fcc Ni crystallites) is predominant for all cases.
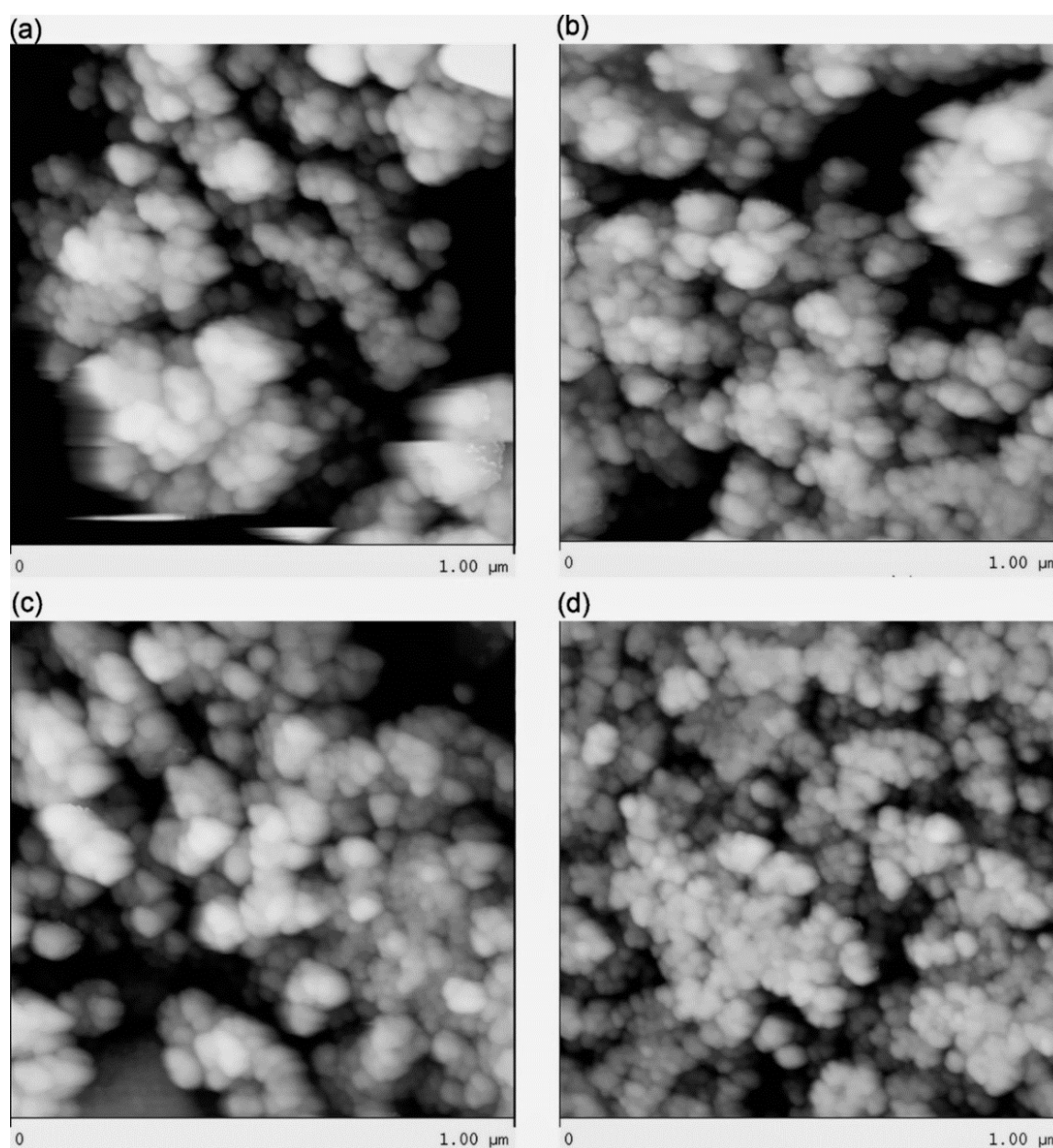


**Fig. 2.** AFM images of silica – Ni/carbon composites: (*a*) CS–Ni–0, (*b*) CS–Ni–0.5, (*c*) CS–Ni–1.0, and (*d*) CS–Ni–2.5
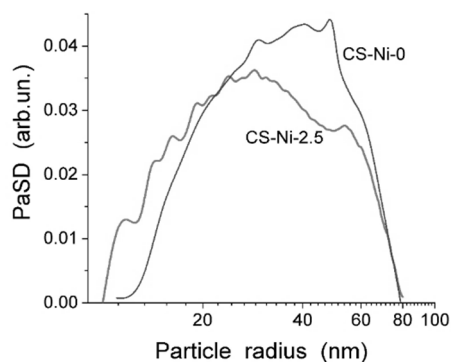
**Fig. 3.** Particle size distributions computed using AFM images with ImageJ software (Granulometry plugin) for two boundary samples: CS–Ni–0 and CS–Ni–2.5
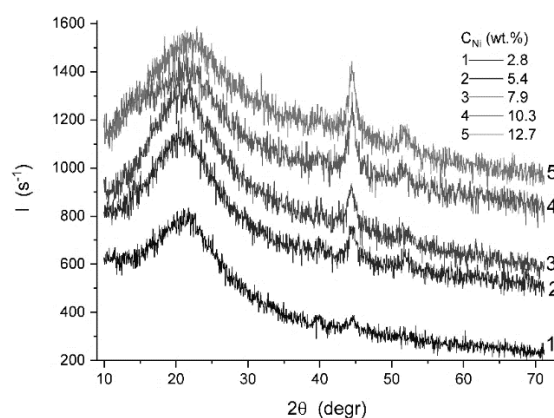


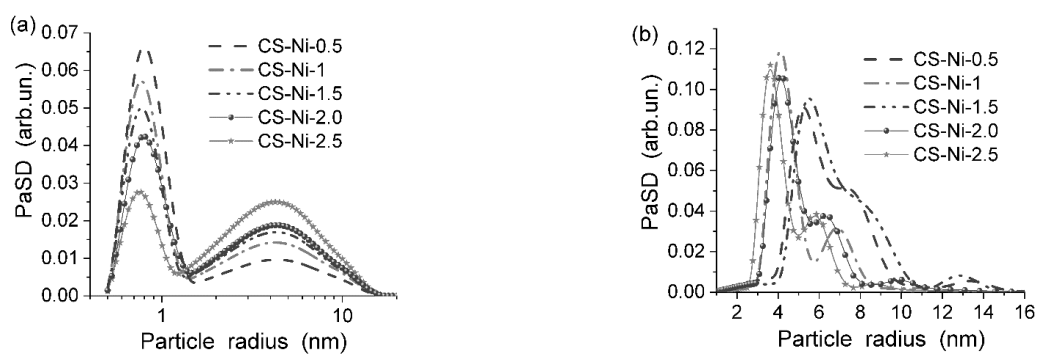**Fig. 4.** XRD patterns for silica – Ni/carbon composites



**Fig. 5.** Particle size distributions computed using XRD patterns for (*a*) amorphous phases with silica and carbon and (*b*) Ni crystallites

**Table 2.** Contribution of particles of lamellar ($C_{lam}$), cylindrical ($C_{cyl}$), and spherical ($C_{sph}$) shapes (XRD/SCR procedure)

| Sample | Amorphous carbon/silica | | | Ni crystallites | | |
|---|---|---|---|---|---|---|
| | $C_{lam}$ | $C_{cyl}$ | $C_{sph}$ | $C_{lam}$ | $C_{cyl}$ | $C_{sph}$ |
| CS–Ni–0.5 | 0.177 | 0.118 | 0.705 | 0.119 | 0.118 | 0.767 |
| CS–Ni–1 | 0.250 | 0.183 | 0.567 | 0.053 | 0.067 | 0.880 |
| CS–Ni–1.5 | 0.275 | 0.234 | 0.491 | 0.043 | 0.087 | 0.870 |
| CS–Ni–2 | 0.295 | 0.266 | 0.439 | 0.088 | 0.090 | 0.822 |
| CS–Ni–2.5 | 0.398 | 0.354 | 0.248 | 0.038 | 0.058 | 0.904 |

The Raman spectra of composites (Fig. 6) show that the D ($sp^3$ structures at 1400–1300 cm$^{-1}$) and G ($sp^2$ structures at 1600 cm$^{-1}$) bands, as well as much weaker bands at higher (3500–2000 cm$^{-1}$) and lower (900–150 cm$^{-1}$) shifts, depend on the Ni content affecting the carbon organization, especially of the $sp^3$ structures. The Raman spectra (Figs. 6 and 7) show that a shape and contribution of the D line (increasing with $C_{Ni}$) depend on the Ni content more strongly than that of the G band. Note that a significant degree of burn–off of activated carbon (AC) does not practically change the D/G ratio in comparison to the related char (Fig. 7). The Raman spectroscopy results (Figs. 6 and 7) are in agreement with the XRD data (Fig. 5) since contribution of larger amorphous carbon structures, less ordered, increases with increasing Ni content (Fig. 6, spectrum 6 for CS–Ni–2.5).
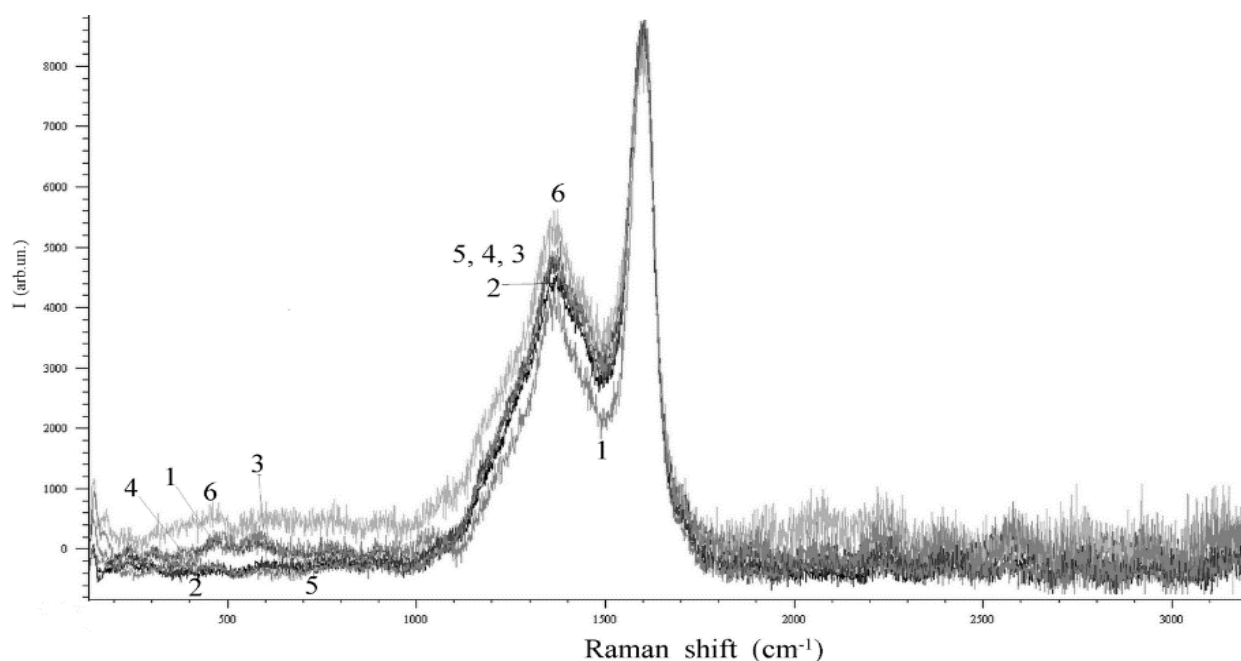


**Fig. 6.** Raman spectra of silica – Ni/carbons composites CS–Ni–X at X = (*1*) 0, (*2*) 0.5, (*3*) 1.0, (*4*) 1.5, (*5*) 2.0, and (*6*) 2.5
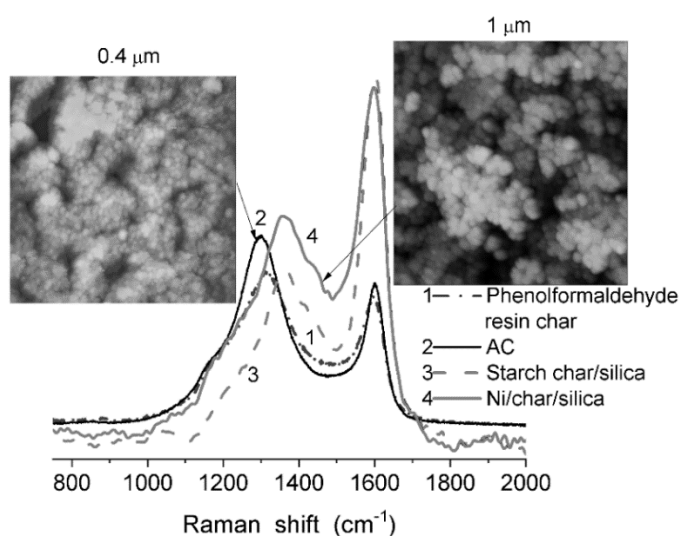


**Fig. 7.** Comparison of Raman spectra for silica – Ni/carbon composites (CS–Ni–0 and CS–Ni–2.5) and phenolformaldehyde resin char and related activated carbon (AC)

**Table 3.** Textural characteristics of adsorbents studied (DFT SCV/SCR)

| Sample | $S_{BET}$ (m²/g) | $S_{NLDFT}$ (m²/g) | $V_p$ (cm³/g) | $V_{nano}$ (cm³/g) | $V_{meso}$ (cm³/g) | $V_{macro}$ (cm³/g) | $S_{nano}$ (m²/g) | $S_{meso}$ (m²/g) | $S_{macro}$ (m²/g) | $<R_V>$ (nm) | $<R_S>$ (nm) | $\Delta w$ (%) | $c_{slit}$ | $c_{cyl}$ | $c_{sph}$ |
|---|---|---|---|---|---|---|---|---|---|---|---|---|---|---|---|
| Si–50 | 503 | 443 | 1.292 | 0.095 | 0.980 | 0.217 | 255 | 235 | 13 | 15.0 | 5.1 | 3.1 | – | 1 | – |
| CS–Ni–0 | 292 | 323/271 | 0.887 | 0.111 | 0.658 | 0.118 | 184 | 105 | 4 | 13.5 | 3.1 | 4.3 | 0.941 | 0.014 | 0.045 |
| CS–Ni–0.5 | 326 | 351/301 | 0.982 | 0.123 | 0.727 | 0.131 | 201 | 121 | 4 | 13.3 | 3.1 | 3.2 | 0.943 | 0.008 | 0.049 |
| CS–Ni–1 | 330 | 329/303 | 1.068 | 0.122 | 0.792 | 0.155 | 193 | 130 | 5 | 14.3 | 3.4 | 1.2 | 0.916 | 0.079 | 0.005 |
| CS–Ni–1.5 | 322 | 312/299 | 1.046 | 0.122 | 0.797 | 0.127 | 183 | 135 | 5 | 12.5 | 3.3 | –4.7 | 0.898 | 0.101 | 0.001 |
| CS–Ni–2 | 322 | 305/296 | 0.977 | 0.112 | 0.718 | 0.147 | 177 | 139 | 6 | 14.2 | 3.5 | –0.6 | 0.804 | 0.183 | 0.013 |
| CS–Ni–2.5 | 320 | 305/296 | 1.000 | 0.117 | 0.752 | 0.131 | 175 | 140 | 5 | 12.8 | 3.3 | –5.8 | 0.829 | 0.166 | 0.005 |

Note. The first and second values in $S_{NLDFT}$ correspond to models with cylindrical and slit/cylindrical pores in silica and carbon, respectively. The $V_{nano}$ and $S_{nano}$ values were calculated by integration of the $f_V(R)$ and $f_S(R)$ function, respectively, at 0.35 nm < R < 1 nm, $V_{meso}$ and $S_{meso}$ at 1 nm < R < 25 nm, and $V_{macro}$ and $S_{macro}$ at 25 nm < R < 100 nm. $<R_X> = \int_{R_{min}}^{R_{max}} R f_X(R) dR / \int_{R_{min}}^{R_{max}} f_X(R) dR$ are the average pore radii with respect to the pore volume (X=V) and surface area (X=S).

$\Delta w = (S_{BET} / \int_{R_{min}}^{R_{max}} f_S(R) dR - 1) \times 100$ is the DFT SCV/SCR model error. The values of $c_{slit}$ and $c_{sph}$ correspond to contributions of slit-shaped pores and voids between spherical particles of carbon and $c_{cyl}$ determines contributions of cylindrical pores in silica.
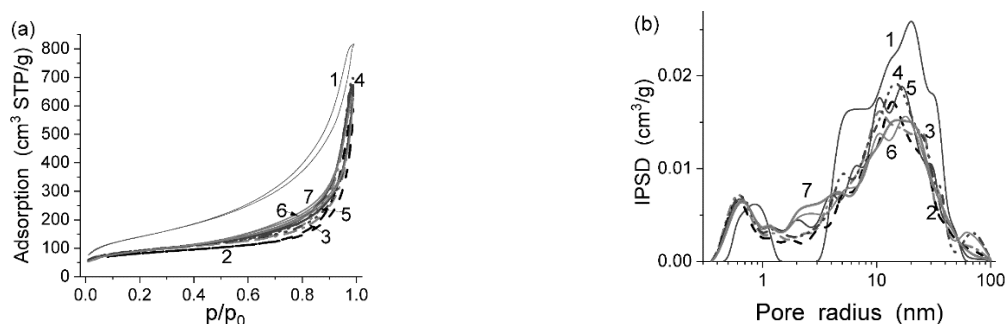
**Fig. 8.** (*a*) Nitrogen adsorption–desorption isotherms and (*b*) incremental pore size distributions (DFT SCV/SCR for pores in silica (cylindrical) and carbon (slit pores and voids between spherical nanoparticles) phases) for Si–50 (curve *1*) and CS–Ni–X at X = (*2*) 0, (*3*) 0.5, (*4*) 1.0, (*5*) 1.5, (*6*) 2.0, and (*7*) 2.5
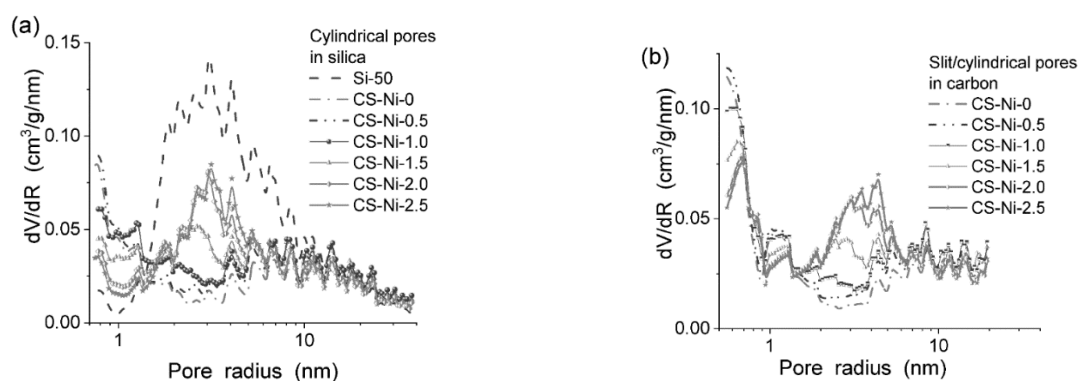


**Fig. 9.** Differential NLDFT PSD with an equilibrium model of (*a*) cylindrical pores in silica and (*b*) slit/cylindrical pores in carbon for Si–50 and composites

On the basis of the textural analysis, one could conclude that the presence of nickel salt during starch carbonization results in an increase in the specific surface area (Table 3, $S_{BET}$) and pore volume ($V_p$) in comparison to the sample CS–Ni–0 prepared without nickel. There is a weak tendence in decreasing $S_{BET}$, $S_{NLDFT}$, $S_{nano}$, and $S_{meso}$ values with increasing Ni content (Table 3). However, the values of $V_p$ and its components ($V_{nano}$, $V_{meso}$, and $V_{macro}$) are larger for CS–Ni–X (X = 0.5–2.5) than for CS–Ni–0 (Table 3). However, their changes *vs.* $C_{Ni}$ are non–monotonic. These results could be explained by several factors (mentioned above) affecting the morphology, structure, and texture of the C/Ni deposits. These factors differently affect the nitrogen adsorption/desorption isotherms (Fig. 8 *a*) and PSD (both differential and incremental) *vs.* $C_{Ni}$ (Figs. 8 *b*, 9, and 10).

The textural characteristics of composites are lower than those of initial Si–50 (Table 3, Figs. 8–10). This could be caused by, at least, two effects: (i) blocking of pore entrance by C/Ni particles, and (ii) formation of deposits in pores.

Silica Si–50 is characterized by a broad PSD. Therefore, narrow pores could be blocked by the C/Ni particles. A portion of smaller C/Ni particles could be located in broader pores. Therefore, a maximal loss of the $S_{BET}$ value for CS–Ni–0 is about 42 %, but the pore volume loss is about 31 %, because contribution of narrow pores into $S_{BET}$ is predominant in contrast to contribution into the pore volume (Table 3). Therefore, one could assume that the blocking effect is predominant. Note that the value of $<R_V> > <R_S>$ (Table 3) and both values decrease in comparison with those for Si–50. However, $<R_V>$ is minimal at maximal $C_{Ni}$, but $<R_S>$ is minimal at minimal $C_{Ni}$. This suggest that a fraction of the deposits is formed in broad pores of silica. Differential and incremental PSD (Figs. 8–10) show features, which are similar to changes in the $<R_S>$ and $<R_V>$ values, respectively.

The differential PSD *dV/dR* give the rate of changes in the pore volume *vs.* pore size, but incremental PSD *ΔV vs. R* show the pore volume at certain pore radius. An increase in the $C_{Ni}$ value leads to decrease in contribution of carbon

structures (slit–shaped pores, $c_{slit}$ in Table 3) and an increase in contribution of cylindrical pores in silica (Table 3, $c_{cyl}$) in total porosity. However, for all composites $c_{slit} > c_{cyl}$. This result could be interpreted as distribution of C/Ni in pores and at a surface of Si–50 globules. Additionally, the carbon phase is porous, because, *e.g.*, for CS–Ni–2.5, contribution of cylindrical pores in silica and outer surface of C/Ni particles can give only about 100 m$^2$/g, *i.e.*, the porosity in carbons should provide a contribution into the total specific surface area about 200 m$^2$/g.
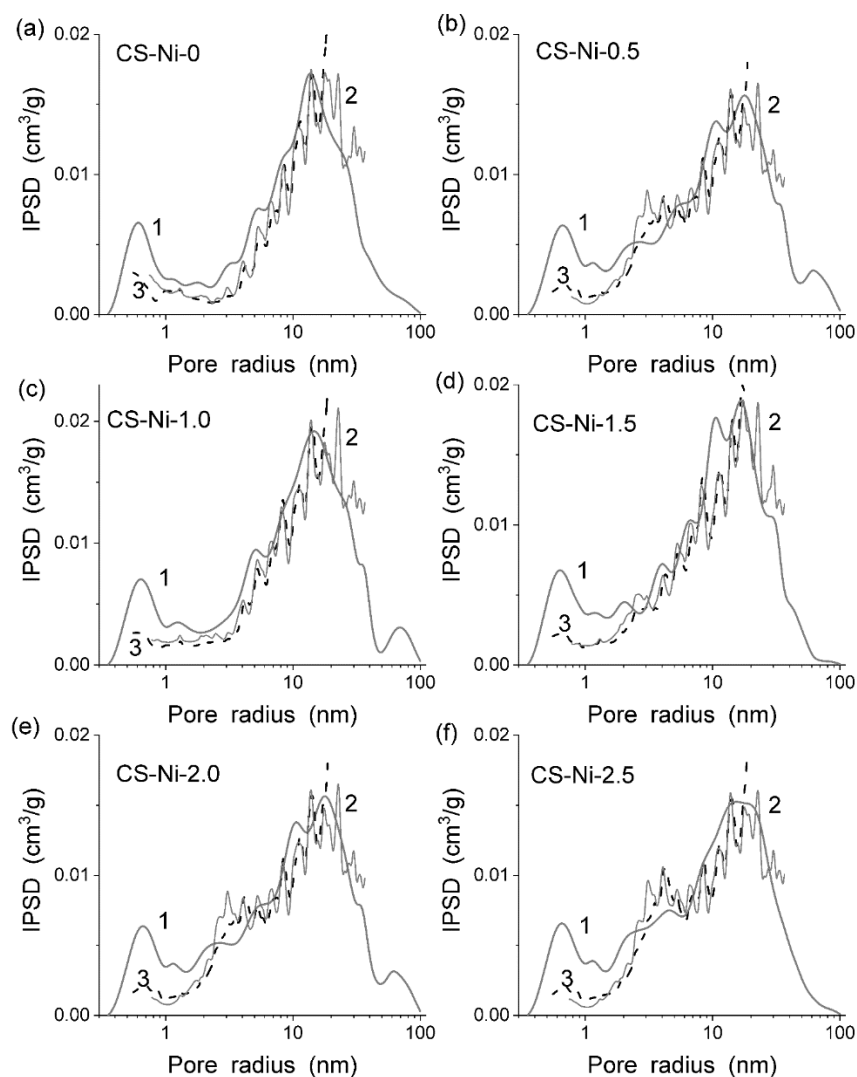


**Fig. 10.** Comparison of incremental PSD computed using DFT SCV/SCR (solid lines *1*) and NLDFT (curves *2* – cylindrical pores in silica and *3* – slit/cylindrical pores in carbon) for composites SC–Ni–X at X = (*a*) 0, (*b*) 0.5, (*c*) 1.0, (*d*) 1.5, (*e*) 2.0, and (*f*) 2.5

It is of interest to analyze the texture of Si–50 in detail since it affects the deposit structure. Precipitated silica Si–50 and fumed silica A–500 ($S_{BET}$ = 492 m$^2$/g, $V_p$ = 0.874 cm$^3$/g) are characterized by similar $S_{BET}$ values but different bulk density ($\rho_b$ = 0.175 and 0.050 g/cm$^3$) and pore volumes. These $\rho_b$ values correspond to different empty volumes ($V_{em}$ = $1/\rho_b$ – $1/\rho_0$, were $\rho_0$ is the true density of amorphous silica ≈ 2.2 g/cm$^3$) of the powders $V_{em}$ = 5.26 and 19.54 cm$^3$/g, respectively. However, stronger packing of nanoparticles in Si–50 globules (~50 μm in size) than in loose nanoparticle aggregates of A–500 results in more effective filling of mesopores and narrow macropores of Si–50 by nitrogen (Fig. 11). As a whole,

precipitated silica is similar to hydro–compacted nanosilicas [72]. These features of the particulate morphology and texture of Si–50 can affect the distribution of carbon/Ni deposits at a surface and in pores of silica globules.
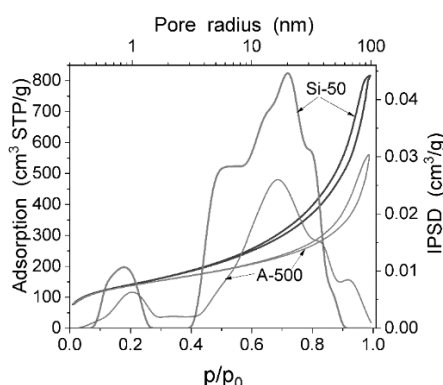


**Fig. 11.** Comparison of nitrogen adsorption isotherms and IPSD DFT for Si–50 and fumed silica A–500 with similar $S_{BET}$ values

According to [73], *p*–nitrophenol (pNP) is poorly adsorbed onto intact silica surface, but it is well adsorbed onto carbons or carbonaceous fragments of carbon/silica (carbosil) composites. For different kinds of carbons, the quantity of adsorbed pNP per a surface unit can be similar if narrow nanopores are absent. The pNP adsorption onto composites (Fig. 12) could be applied to determine: the specific surface area of carbon deposits *per se*

$$S_C^{cs} = \frac{a^{cs} S^s - a^s S^{cs}}{a_{mon}^{cb} S^s - a^s},$$ (4)

where $a^{cs}$ is the amount of monolayer adsorption of pNP onto carbosil (g pNP/g carbosil), $a_{mon}^{cb}$ is the amount of monolayer adsorption of pNP onto graphitized carbon black ($5.28 \times 10^{-4}$ g/m²), $S_C^{cs}$ is the surface area of carbon (m²/g), $S^s$ is the total surface area of silica (m²/g), $a^s$ is the amount of pNP adsorbed onto a silica surface at a concentration corresponding to monolayer adsorption on carbosil (g pNP/g silica). Then, the specific surface area of carbon deposits could be calculated

$$S_C = S_C^{cs}(100 / C_C)$$ (5)

where $C_C$ is the content (wt. %) of carbon deposits. The degree of silica surface coverage by carbon deposits is

$$P_C = \frac{S_C^{cs}}{S^{cs}} 100\% \cdot$$ (6)

The average diameter of deposit particles could be estimated using a model of spherical C/Ni particles

$$D = \frac{6000}{\rho S_{C/Ni}} \text{ [nm]},$$ (7)

where $\rho$ is the true density of deposit particles with a carbon shell ($\rho_C = 1.8$ g/cm³) and a nickel core ($\rho_{Ni} = 8.902$ g/cm³), and

$$\rho = \rho_C \times C_C/(C_C + C_{Ni}) + \rho_{Ni} \times C_{Ni}/(C_C + C_{Ni}).$$ (8)

The structural values (Table 4), estimated from the pNP adsorption data (Fig. 12), differ from the characteristics, estimated from the nitrogen adsorption (Table 3) and AFM images (Figs. 2 and 3) due to several factors: (i) N₂ molecule is much smaller than O₂NC₆H₄OH (*e.g.*, the occupied surface area is $\sigma_0 = 0.162$ and 0.525 nm² [74], respectively, and the wdW thickness of N₂ is lower, at least, by two times because of easy rotation of both functional groups of pNP); therefore, surface area and a part of nanopores accessible for the probes strongly differ; (ii) the surface area occupied by probe molecules can differently depend on the surface structure of composites (*e.g.*, the orientation effects for N₂ at a silica surface reduce the $\sigma_0$ value to 0.137 nm², but for pNP, it could be 0.25 nm²); (iii) adsorption of pNP molecules in complex pores with different composition of pore walls (*e.g.*, one wall is with silica but another one is with carbon) is poorly determined in the

Kamegawa – Yoshida model; and (iv) the presence of possible systematic errors in treatment models of the experimental data. For example, the PaSD (Fig. 3) and *D* values (Table 4) give different results for composites, and this difference is larger for CS–Ni–0 than for CS–Ni–2.5 that is unexpected because the Kamegawa – Yoshida model is developed for carbon/silica composites but not for carbon/metal/silica composites. Note that the

difference in the pNP adsorption calculated per m$^2$ (Fig. 12 *b*) is larger than that per gram (Fig. 12 *a*), *e.g.*, for CS-Ni-0 and CS-Ni-0.5. However, for samples with greater amounts of Ni, there is the opposite effect (the difference is larger for the pNP adsorption per gram of sorbents). These results confirm that appropriate characterization of complex systems is possible if several methods are used in parallel to check and compare obtained results.

**Table 4.** Structural parameters of carbon deposits bused on the pNP adsorption data

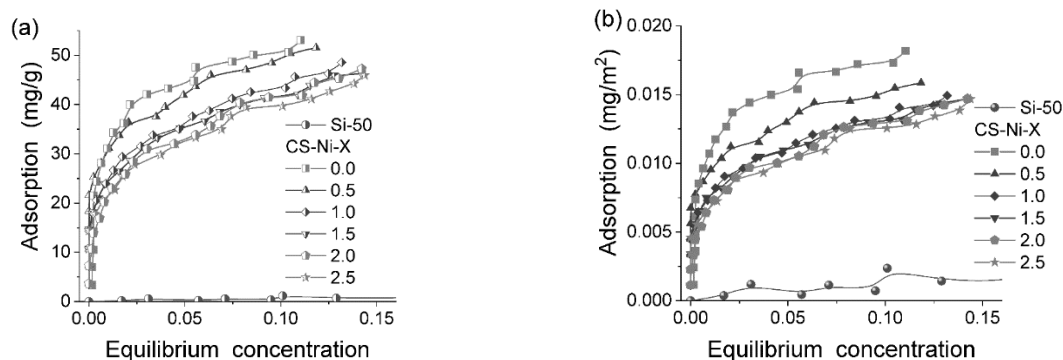| Sample | $S_C^{cs}$ (m²/g) | $P_C$ (%) | $S_C$ (m²/g) | $D$ (nm) |
|---|---|---|---|---|
| CS–Ni–0 | 11.55 | 3.96 | 64.20 | 51.92 |
| CS–Ni–0.5 | 10.60 | 3.25 | 55.88 | 39.34 |
| CS–Ni–1.0 | 10.23 | 3.11 | 67.35 | 29.33 |
| CS–Ni–1.5 | 9.84 | 3.06 | 68.57 | 25.00 |
| CS–Ni–2.0 | 10.23 | 3.19 | 86.77 | 20.98 |
| CS–Ni–2.5 | 9.66 | 3.02 | 84.29 | 19.45 |



**Fig. 12.** Adsorption isotherms of *p*–nitrophenol on composites measured in (*a*) mg/g and (*b*) mg/m² *vs.* $c_{eq.pNP}$ (in g/L)

## CONCLUSION

Precipitated silica Sipernat 50 globules (~50 μm in size) are characterized by a broad pore size distribution. Therefore, Ni/char deposits can be located at a surface of silica microglobules (blocking a fraction of narrow pores) or in broad mesopores and macropores. The first type of Ni/C location causes decreasing specific surface area without a significant shift of the PSD peaks. The second type of deposit location leads to decreasing pore volume with certain shifts of the PSD peaks. An increase in the amounts of Ni leads to decreasing of all textural characteristics calculated per gram of an adsorbent because not only of pore infilling and blocking but also due to high true density of nickel $\rho_{Ni} \approx 8.9$ g/cm³.

However, for char, there is the opposite effects of the true density because of $\rho_C < \rho_{SiO2}$. On the other hand, a decrease in the textural characteristics is maximal for char without Ni. This can be explained by (i) the Ni catalytic effects since metal nuclei provide the centers of char formation (this change the char location); and (ii) larger amounts of carbons in samples CS–Ni–X at X ≥ 1 that provide an increase in the surface area of the carbon phase (according to pNP adsorption data) with changes in the location of the deposit particles at the surface of silica globules. The presence of the nickel phase could result in the formation of smaller (according to AFM image analysis) but more densely packed (according to the adsorption and XRD data) char nanoparticles. Estimation of possible contribution of pores

accessible for nitrogen molecules in silica globules and outer surface of carbon/Ni particles suggests that the carbon phase is porous that provides a significant part of the specific surface area of the composites. However, a part of narrow pores in char is inaccessible for NPN molecules. Therefore, the estimation of the specific surface area of char per se using the PNP adsorption could give underestimated textural characteristics. Amorphous silica and char phases are characterized by the presence of certain nuclei of radius < 1 nm and 2 nm < $R$ < 10 nm estimated from the XRD patterns using full peak profile analysis with a self–consistent regularization procedure and a complex model of particle shapes. The Ni crystallites are of several sizes, since particle size distributions include two–three peaks in the 3–13 nm range in radius. The Raman spectra show that the main changes with increasing Ni content are characteristic to $sp^3$ carbon structures (D line) in contrast to the $sp^2$ structures (G line). The pore size distributions (both differential and incremental) demonstrate complex changes in a broad size range due to increasing Ni content in composites. As a whole, changes in the Ni content in nanostructured C/Ni/silica composites allow one to control the morphological, structural, and textural characteristics of the whole materials.

## ACKNOWLEDGEMENTS

# Наноструктуровані композити на основі осадженого кремнезему та кристалітів Ni, вкритих вуглецем із карбонізованого крохмалю

**В.М. Гунько, Б. Хармас, Я. Скубішевська–Земба**

*Інститут хімії поверхні ім. О.О. Чуйка Національної академії наук України*
*вул. Генерала Наумова, 17, Київ, 03164, Україна, vlad_gunko@ukr.net*
*Хімічний факультет, Університет Марії Кюрі–Склодовської*
*пл. Марії Кюрі–Склодовської, 3, Люблін, 20–031, Польща*

*Гібридні композити вуглець/метал/оксиди металу (металоїду) можуть бути більш ефективними адсорбентами для низько– та високомолекулярних сполук, полярних та неполярних, газоподібних та рідких. Наявність металевих нанокристалітів і вуглецевих наноструктур може забезпечити каталітичні властивості в окисно–відновних реакціях. Для більш ефективного використання гібридних композитів необхідно контролювати їхні морфологічні, структурні, текстурні та адсорбційні характеристики, щоб вони відповідали цільовим застосуванням. Тому метою даного дослідження був синтез наноструктурованих композитів вуглець/метал/кремнезем із змінним вмістом металу (Ni) для контролю зазначених характеристик. Як матрицю обрано осаджений кремнезем Sipernat 50. Як попередник вуглецю використовували картопляний крохмаль. Як прекурсор наночастинок Ni використовували різну кількість солі Ni(NO₃)₂·6H₂O. Після карбонізації крохмалю та відновлення Ni досліджували набір зразків C/Ni/кремнезем за допомогою атомно–силової мікроскопії, рентгенівської дифракції, рентгенівської флуоресцентної спектроскопії, адсорбції азоту, термогравіметрії та рамановської спектроскопії. Присутність фази нікелю призводить до утворення менших, але більш щільно упакованих наночастинок вуглецю. Оцінка можливого внеску пор, доступних для молекул азоту в глобулах кремнезему та на зовнішній поверхні частинок вуглецю/Ni, свідчить про те, що вуглецева фаза є пористою, що забезпечує значну частину питомої поверхні композиту. Фази аморфного кремнезему та вугілля характеризуються наявністю певних зародків з радіусом < 1 нм і 2 нм < R < 10 нм, оцінених на основі рентгенограм за допомогою аналізу повних піків із процедурою самоузгодженої регуляризації. Кристаліти Ni мають кілька розмірів, оскільки розподіл частинок за розмірами включає два–три піки в діапазоні 3–13 нм в радіусі. Спектри КРС показують, що основні зміни зі збільшенням вмісту Ni характерні для вуглецевих структур sp³ (лінія D) на відміну від структур sp² (лінія G). Розподіли розмірів пор (як диференціальні, так і інкрементні) демонструють складні зміни в широкому діапазоні розмірів через збільшення вмісту Ni в композитах. Загалом зміни вмісту Ni у наноструктурованих композитах*

*C/Ni/кремнезем дозволяють керувати морфологічними, структурними та текстурними характеристиками матеріалів.*

**Ключові слова**: *осаджений кремнезем, крохмаль, нітрат нікелю, Ni нанокристаліти, вкриті вуглецем частинки Ni, структурні характеристики*

# REFERENCES

1. Somasundaran P. (Ed.) *Encyclopedia of Surface and Colloid Science*. Third Edition. (Boca Raton: CRC Press, 2015).
2. Ahuja S. (Ed.) *Separation Science and Technology*, V. 15. (Amsterdam: Elsevier, 2022).
3. Hussain C.M. (Ed.) *Handbook of Polymer Nanocomposites for Industrial Applications*. (Amsterdam: Elsevier, 2021).
4. Ahmad A., Kumar R., Jawaid M. (Eds.) *Emerging Techniques for Treatment of Toxic Metals from Wastewater*. (Amsterdam: Elsevier, 2022).
5. Singh S., Kumar P., Mondal D.P. (Eds.) *Advanced Ceramics for Versatile Interdisciplinary Applications*. (Amsterdam: Elsevier, 2022).
6. Ngu L.H. *Carbon Capture Technologies*. (Amsterdam: Elsevier, 2022).
7. Yang R.T. *Adsorbents: Fundamentals and Applications*. (New York: Wiley, 2003).
8. Birdi K.S. (Ed.) *Handbook of Surface and Colloid Chemistry*. Third edition. (Boca Raton: CRC Press, 2009).
9. *Ullmann's Encyclopedia of Industrial Chemistry*. (Weinheim: Wiley–VCH, 2008).
10. Lu K. *Nanoparticulate Materials. Synthesis, Characterization, and Processing*. (Hoboken, New Jersey: John Wiley & Sons, Inc., 2013).
11. Moreno–Piraján J.C., Giraldo–Gutierrez L., Gómez–Granados F. *Porous Materials Theory and Its Application for Environmental Remediation*. (Cham: Springer Nature, 2021).
12. Rousseau R.W. *Handbook of Separation Process Technology*. (New York: John Wiley & Sons, 1987).
13. Gun'ko V.M., Turov V.V. *Nuclear Magnetic Resonance Studies of Interfacial Phenomena*. (Boca Raton: CRC Press, 2013).
14. Leboda R. Carbon–mineral adsorbents – new type of sorbents. Part I. The methods of preparation. *Mater. Chem. Phys.* 1992. **31**: 243. Part II. Surface properties and methods of their modification *Mater. Chem. Phys.* 1993. **34**: 123.
15. Chan Z., Miao F., Xiao Z., Juan H., Hongbing Z. Effect of doping levels on the pore structure of carbon nanotube/silica xerogel composites. *Mater. Lett.* 2007. **61**(3): 644.
16. Lavorgna M., Romeo V., Martone A., Zarrelli M., Giordano M., Buonocore G.G., Qu M.Z., Fei G.X., Xia H.S. Silanization and silica enrichment of multiwalled carbon nanotubes: Synergistic effects on the thermal–mechanical properties of epoxy nanocomposites. *Eur. Polym. J.* 2013. **49**(2): 428.
17. Othman R.N., Kinloch I.A., Wilkinson A.N. Synthesis and characterisation of silica–carbon nanotube hybrid microparticles and their effect on the electrical properties of poly(vinyl alcohol) composites. *Carbon.* 2013. **60**: 461.
18. Choi S., Kim K., Nam J., Shim S.E. Synthesis of silica–coated graphite by enolization of polyvinylpyrrolidone and its thermal and electrical conductivity in polymer composites. *Carbon.* 2013. **60**: 254.
19. Chu Y.–H., Yamagishi M., Wang Z.–M., Kanoh H., Hirotsu T. Adsorption characteristics of nanoporous carbon–silica composites synthesized from graphite oxide by a mechanochemical intercalation method. *J. Colloid Interface Sci.* 2007. **312**(2): 186.
20. Wang Z.–M., Shishibori K., Hoshinoo K., Kanoh H., Hirotsu T. Examination of synthesis conditions for graphite–derived nanoporous carbon–silica composites. *Carbon.* 2006. **44**: 2479.
21. Kumagai S., Ishizawa H., Aoki Y., Toida Y. Molded micro– and mesoporous carbon/silica composite from rice husk and beet sugar. *Chem. Eng. J.* 2010. **156**(2): 270.
22. Tso C.Y., Chao C.Y.H. Activated carbon, silica–gel and calcium chloride composite adsorbents for energy efficient solar adsorption cooling and dehumidification systems. *Int. J. Refrig.* 2012. **35**(6): 1626.
23. Ye L., Ji Z.–H., Han W.–J., Hu J.–D., Zhao T. Synthesis and characterization of silica/carbon composite aerogels. *J. Am. Ceram. Soc.* 2010. **93**(4): 1156.
24. Furtado A.M.B., Wang Y., LeVan M.D. Carbon silica composites for sulfur dioxide and ammonia adsorption. *Microporous Mesoporous Mater.* 2013. **165**: 48.

25. Glover T.G., LeVan M.D. Carbon–silica composite adsorbent: Sensitivity to synthesis conditions. *Microporous Mesoporous Mater.* 2009. **118**(1–3): 21.

26. Valle–Vigón P., Sevilla M., Fuertes A.B. Carboxyl–functionalized mesoporous silica–carbon composites as highly efficient adsorbents in liquid phase. *Microporous Mesoporous Mater.* 2013. **176**: 78.

27. Santa C.F., Jaber M., Guth J.L., Sierra L. Synthesis of texturally biphasic mesoporous carbon–silica composites and carbons. *Microporous Mesoporous Mater.* 2013. **173**: 53.

28. Lua A.C., Shen Y. Preparation and characterization of polyimide–silica composite membranes and their derived carbon–silica composite membranes for gas separation. *Chem. Eng. J.* 2013. **220**: 441.

29. Sanchez F., Ince C. Microstructure and macroscopic properties of hybrid carbon nanofiber/silica fume cement composites. *Compos. Sci. Technol.* 2009. **69**(7–8): 1310.

30. Zhou X., Shi T. One–pot hydrothermal synthesis of a mesoporous $SiO_2$–graphene hybrid with tunable surface area and pore size. *Appl. Surf. Sci.* 2012. **259**: 566.

31. Tang J., Wang T., Sun X., Hu Y., Xie Q., Guo Y., Xue H., He J. Novel synthesis of reduced graphene oxide–ordered mesoporous carbon composites and their application in electrocatalysis. *Electrochim. Acta*. 2013. **90**: 53.

32. Manocha L.M., Manocha S., Patel K.B., Glogar P. Oxidation behaviour of carbon/carbon composites impregnated with silica and silicon oxycarbide. *Carbon*. 2000. **38**(10): 1481.

33. Nandan D., Sreenivasulu P., Sivakumar Konathala L.N., Kumar M., Viswanadham N. Acid functionalized carbon–silica composite and its application for solketal production. *Microporous Mesoporous Mater.* 2013. **179**: 182.

34. Xu H., Zhang H., Huang Y., Wang Y. Porous carbon/silica composite monoliths derived from resorcinol–formaldehyde/TEOS. *J. Non–Crystal. Solid.* 2010. **356**(20–22): 971.

35. Charmas B. Characterization of porosity and thermal properties of Ni–doped carbosils obtained by starch gelation. *Adsorpt. Sci. Technol*. 2015. **33**(6–8): 539.

36. Herath A., Navarathna C., Warren S., Perez F., Pittman C.U. Jr., Mlsna T.E. Iron/titanium oxide–biochar ($Fe_2TiO_5$/BC): A versatile adsorbent/photocatalyst for aqueous Cr(VI), $Pb^{2+}$, $F^-$ and methylene blue. *J. Colloid Interface Sci.* 2022. **614**: 603.

37. Wang J., Han Q., Wang K., Li S., Luo W., Liang Q., Zhong J., Ding M. Recent advances in development of functional magnetic adsorbents for selective separation of proteins/peptides. *Talanta*. 2023. **253**: 123919.

38. Nirenjan Shenoy P.N., Arjun N.M., Senthil Kumar P., Sree Hari A.B., Nithya K., Asha Sathish P. Recycled mesoporous magnetic composites with high surface area derived from plastic and de–oiled sludge wastes: An empirical comparison on their competitive performance for toxic Cr (VI) removal. *Chemosphere*. 2022. **292**: 133375.

39. Salama A., Abou–Zeid R.E., Ionic chitosan/silica nanocomposite as efficient adsorbent for organic dyes. *Inter. J. Bio. Macromol.* 2021. **188**: 404.

40. Meti P., Mahadik D.B., Lee K.–Y., Wang Q., Kanamori K., Gong Y.–D., Park H.–H. Overview of organic–inorganic hybrid silica aerogels: Progress and perspectives. *Mater. Des.* 2022. **222**: 111091.

41. Juela D.M. Promising adsorptive materials derived from agricultural and industrial wastes for antibiotic removal: A comprehensive review. *Sep. Purif. Technol*. 2022. **284**: 120286.

42. Ounphikul B., Chantarasombat N., Hunt A.J., Ngernyen Y. A new low–cost carbon–silica composite adsorbent from a by–product of the sugar industry. *Mater. Today: Proc.* 2022. **51**(5): 1884.

43. El Kurdi R., Chebl M., Sillanpää M., El–Rassy H., Patra D. Chitosan oligosaccharide/silica nanoparticles hybrid porous gel for mercury adsorption and detection. *Materials Today Commun.* 2021. **28**: 102707.

44. Ighalo J.O., Omoarukhe F.O., Ojukwu V.E., Iwuozor K.O., Igwegbe C.A. Cost of adsorbent preparation and usage in wastewater treatment: A review. *Cleaner. Chem. Eng.* 2022. **3**: 100042.

45. Gun'ko V.M., Matkovsky A.K., Charmas B., Skubiszewska–Zięba J., Pasieczna–Patkowska S. Carbon–silica gel adsorbents: effects of matrix structure and carbon content on adsorption of polar and nonpolar adsorbates. *J. Therm. Anal. Calorim*. 2017. **128**(3): 1683.

46. Leboda R., Turov V.V., Charmas B., Skubiszewska–Zięba J., Gun'ko V.M. Surface properties of mesoporous carbon–silica gel adsorbents. *J. Colloid Interface Sci.* 2000. **223**(1): 112.

47. Gun'ko V.M., Leboda R., Skubiszewska–Zięba J., Rynkowski J. Silica gel modified due to pyrolysis of acetylacetone or metal (Ti, Cr, Co, Ni, Zn, Zr) acetylacetonates. *J. Colloid Interface Sci.* 2000. **231**(1): 13.

48. Gun'ko V.M., Leboda R., Turov V.V., Villiéras F., Skubiszewska–Zięba J., Chodorowski S., Marciniak M. Structural and energetic nonuniformities of pyrocarbon–mineral adsorbents. *J. Colloid Interface Sci.* 2001. **238**(2): 340.

49. Gun'ko V.M., Leboda R., Skubiszewska–Zięba J., Turov V.V., Kowalczyk P. Structure of silica gel Si–60 and pyrocarbon/silica gel adsorbents thermally and hydrothermally treated. *Langmuir*. 2001. **17**(11): 3148.

50. Gun'ko V.M., Leboda R., Pokrovskiy V.A., Charmas B., Turov V.V., Ryczkowski J. A study of the organic carbon content of silica gel carbonised by pyrolysis of alcohols. *J. Anal. Appl. Pyrolysis*. 2001. **60**(2): 233.

51. Skubiszewska–Zięba J., Leboda R., Seledets O., Gun'ko V.M. Effect of preparation conditions of carbon–silica adsorbents based on mesoporous silica gel Si–100 and carbonised glucose on their pore structure. *Colloids Surf. A*. 2003. **231**(1–3): 39.

52. Gun'ko V.M., Skubiszewska–Zięba J., Leboda R., Turov V.V. Impact of thermal and hydrothermal treatments on structural characteristics of silica Gel Si–40 and carbon/silica gel adsorbents. *Colloids Surf. A*. 2004. **235**(1–3): 101.

53. Seledets O., Gun'ko V.M., Skubiszewska–Zięba J., Leboda R., Musiatowicz M., Podkoscielny P., Dabrowski A. Structural and energetic heterogeneities of pyrocarbon/silica gel systems and their adsorption properties. *Appl. Surf. Sci.* 2005. **240**(1–4): 222.

54. Gun'ko V.M., Seledets O., Skubiszewska–Zięba J., Zarko V.I., Leboda R., Janusz W., Chibowski S. Phosphorus–containing carbon deposits on silica gel Si–100. *Microporous Mesoporous Mater.* 2005. **87**(2): 133.

55. Blitz J.P., Gun'ko V.M. (Eds.) *Surface Chemistry in Biomedical and Environmental Science.* NATO Science Series II: Mathematics, Physics and Chemistry. V. 228. (Dordrecht: Springer, 2006).

56. Skubiszewska–Zięba J., Charmas B., Leboda R., Gun'ko V.M. Carbon–mineral adsorbents with a diatomaceous earth/perlite matrix modified by carbon deposits. *Microporous Mesoporous Mater.* 2012. **156**: 209.

57. Tomaszewski W., Gun'ko V.M., Skubiszewska–Zięba J., Charmas B., Leboda R. Influence of carbon deposits and subsequent silylation of silica gel on sorption efficiency of explosive nitramines. *Colloids Surf. A*. 2015. **468**: 76.

58. Tomaszewski W., Gun'ko V.M. Evaluation of adsorption and desorption steps in solid–phase extraction of explosives using carbon/silica gel nanocomposites. *J. Sep. Sci.* 2015. **38**(14): 2488.

59. Gun'ko V.M., Matkovsky A.K., Charmas B., Skubiszewska–Zięba J., Pasieczna–Patkowska S. Carbon–silica gel adsorbents: effects of matrix structure and carbon content on adsorption of polar and nonpolar adsorbates. *J. Therm. Anal. Calorim.* 2017. **128**(3): 1683.

60. Gregg S.J., Sing K.S.W. *Adsorption, Surface Area and Porosity.* 2nd ed. (London: Academic Press, 1982).

61. Adamson A.W., Gast A.P. *Physical Chemistry of Surface.* 6th ed. (New York: Wiley, 1997).

62. Gun'ko V.M. Textural characteristics of composite adsorbents analyzed with density functional theory and self–consistent regularization procedure. *Him. Fiz. Tehnol. Poverhni.* 2020. **11**(2): 163.

63. Gun'ko V.M. Various methods to describe the morphological and textural characteristics of various materials. *Him. Fiz. Tehnol. Poverhni.* 2018. **9**(4): 317.

64. Gun'ko V.M. Morphological and textural features of various materials composed of porous or nonporous nanoparticles differently packed in secondary structures. *Appl. Surf. Sci.* 2021. **569**: 151117.

65. Ravikovitch P.I., Neimark A.V. Density functional theory model of adsorption on amorphous and microporous silica materials. *Langmuir.* 2006. **22**(26): 11171.

66. Gun'ko V.M. Nano/meso/macroporous materials characterization affected by experimental conditions and features of the used methods. *Him. Fiz. Tehnol. Poverhni.* 2020. **11**(1): 5.

67. Gun'ko V.M. Polymer adsorbents vs. functionalized oxides and carbons: particulate morphology and textural and surface characterization. *Polymers.* 2021. **13**(1249): 1.

68. *ImageJ*. Version 1.53t. 2022. https://imagej.nih.gov/ij/, https://imagej.nih.gov/ij/plugins/granulometry.html.

69. Gun'ko V.M., Oranska O.I., Paientko V.V., Sulym I.Ya. Particulate morphology of nanostructured materials. *Him. Fiz. Tehnol. Poverhni.* 2020. **11**(3): 368.

70. Gun'ko V.M., Meikle S.T., Kozynchenko O.P., Tennison S.R., Ehrburger–Dolle F., Morfin I., Mikhalovsky S.V. Comparative characterization of carbon and polymer adsorbents by SAXS and nitrogen adsorption methods. *J. Phys. Chem. C.* 2011. **115**(21): 10727.

71. Gun'ko V.M., Kozynchenko O.P., Tennison S.R., Leboda R., Skubiszewska–Zięba J., Mikhalovsky S.V. Comparative study of nanopores in activated carbons by HRTEM and adsorption methods. *Carbon.* 2012. **50**(9): 3146.

72. Gun'ko V.M., Turov V.V., Pakhlov E.M., Krupska T.V., Charmas B. Effect of water content on the characteristics of hydro–compacted nanosilica. *Appl. Surf. Sci.* 2018. **459**: 171.

73. Kamegawa K., Yoshida H. A method for measuring surface area of carbon of carbon–coated silica gel. *Bull. Chem. Soc. Jpn.* 1990. **63**(12): 3683.

74. Álvarez-Torrellas S., Martin-Martinez M., Gomes H.T., Ovejero G., García J. Enhancement of p-nitrophenol adsorption capacity through $N_2$-thermal-based treatment of activated carbons. *Appl. Surf. Sci.* 2017. **414**: 424.